Bioceramics

THERMAL INTERFACE STRESSES INCLUDING 3D MICROSTRUCTURES IN LAYERED FREE-FORM CERAMICS

Hrishikesh Bale,[a] Jay C. Hanan,[a] James E. Smay[b]
[a]Mechanical and Aerospace Engineering, [b]Chemical Engineering; Oklahoma State University, Stillwater, OK, USA

ABSTRACT

Processing of complex ceramic parts such as a dental restorations involves sintering of ceramic performs. Intended and unintended microstructures such as voids, cracks and, interfaces exist in these parts. These microstructures contribute to the mechanical response and ultimate life. A combined X-ray computed micro-tomography and X-ray micro-diffraction experiment was implemented on an alumina-zirconia layered free-form fabricated composite. The composite serves as a model for examining the mechanics and material characteristics of ceramic dental restorations. The current in-situ X-ray technique is capable of determining the strain values at prescribed spatial locations on the micron scale using high-energy synchrotron radiation and refractive focusing optics.

In coordination with the experimental work, a finite element analysis of the volume generated by micro-tomography was developed. This required implementing a non-trivial procedure of converting the tomograph into a 3D finite element model. Simulation of sintering on this real geometry is compared with the experimental strain results for validation of the model. Once validated, the simulation offers more detailed insight to mechanical properties than experimental measurements offer on their own. This comprehensive procedure of modeling and experimentation including microtomography combined with diffraction offers a powerful method to quantify damage evolution and strain in ceramic layered composites – first intended for dental applications, yet broadly applicable as structural materials.

INTRODUCTION

Two of the ceramics commonly used for dental restorations are alumina and zirconia. Typically they are used independently, but their common sintering temperatures allow combination as laminates or as mixtures. Considerations for choosing these ceramics include fracture toughness, strength, cost, and their aesthetically pleasing color resembling natural teeth. In general, these high-performance ceramics are used as structural members in crowns or bridges and are overlaid with porcelain giving translucence, final color, and texture to the restoration. While they may be sintered together, alumina and zirconia have different mechanical properties such as their elastic moduli and thermal expansion coefficients. These differences in properties provide a source for residual stresses when the two materials are sintered as mixtures or laminates. They superimpose over applied stresses and can accelerate or retard cracking and failure. Under the prolonged or cyclic influence of loads, small cracks grow into larger cracks which are detrimental to the life of the part.[1] This is a serious problem for all bio-material applications whether considering dental restorations or implants and joint replacement prosthesis. Alternatively, the interface layer where the residual stresses exist can be tailored as a low fracture energy region to deflect cracks and induce toughening mechanisms.[2,3] Determination of the residual stresses in such composites and laminates has been a challenging problem. The situation becomes more complicated when intricate geometries are involved, for instance a dental crown.

While experiments providing bulk properties have been extensive, there is a lack of such understanding with composites. This is further complicated by the contribution of micro-scale features such as stress concentrators like pores and facets. Visualization of these defect zones in 3D is possible

using X-ray micro-tomography (μ-CT). Experiments using μ-CT to visualize microstructure and monitor the evolution of the structure have been carried out.[4-6, 7] Such experiments are able to probe in-situ material characteristics and monitor the gradual developments in phase change, pore distribution and, fluid uptake. In addition, efforts to analyze quantitatively properties such as elastic modulus, fracture toughness, and the nature of stresses using X-ray diffraction measurements are ongoing.[8,9,10,11] Both these methods, X-ray micro-diffraction and X-ray micro-tomography, when combined together provide valuable information pertaining to the microstructure and material properties. Some of the preliminary work on the combined experimentation has produced results which evaluate strains from positions which can be tracked by tomography.[12] This gives comprehensive 3D information including spatial coordinates where the particular material property is evaluated.

Pin-pointing stress to a specific location within a 3D volume is important and has been challenging.[13] Finite element simulations are generally utilized in such scenarios, where a model is generated as close as reasonable to the actual geometry. Many times this leads to approximations from the actual result. However, finite element simulations are advantageous since results from any location throughout the sample volume can be observed. The present work refers to an experimental and computational evaluation of alumina-zirconia composites and aims to validate a finite element model which was modeled with actual sample dimensions using tomography as input for constructing the mesh. A comparison of the experimental results and simulations will confirm the effectiveness of both the experimental technique and the simulations.

METHOD

Sample Preparation

The experiment consists of sintered samples produced using a novel solid free form fabrication technique called Robo-casting to assemble layers of alumina and zirconia. Freeform fabrication involves printing colloidal inks of the two ceramics using fine printing tips or nozzles. The 3-D tool path print design is fed to a computer numeric control system to obtain the desired geometry. Following earlier work,[14] the starting inks consisted of alumina, Al_2O_3 (α_{Al2O3}= 5.5 μm/m-°C at 25 °C, 10.1 μm/m-°C at 1127 °C)[15] and Yttria stabilized tetragonal Zircoina, ZrO_2 (CTE_{ZrO2}=10.9 at 25 °C)[15]. Mixtures of the two inks can also be printed. The colloid volume fraction in the inks was ϕ_{solids} = 0.47 for Al_2O_3 and ZrO_2. The green bodies were first bisque fired at 1100°C then sintered at 1450 °C.

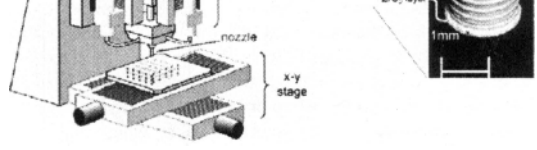

Figure 1. Schematic of robocasting used to fabricate the layered composites. 3-D printing is performed with ink nozzles. One nozzle dedicated to an alumina ink and the other to zirconia. (see also[14]).

Combined *In-Situ* X-Ray Micro-Diffraction and Micro Computed Tomography

The Advanced Photon Source X-ray synchrotron facility at Argonne National Laboratory, Chicago was utilized to conduct the X-ray diffraction and imaging experiments on the abovementioned samples. The beamline 1D-2-BM was modified so both high-resolution tomography and micro diffraction could be conducted in-situ on the composite. The diffraction CCD (Charged Coupled Device), the tomography camera and the sample stage straddles a plane including the X-ray beam. The diffraction CCD is oriented at a 2θ angle of 30° to the beam. The camera used for tomography is mounted with a scintillator plate that fluoresces X-rays as visible light. A high-precision translation stage was used to position the sample with respect to the X-ray beam.

Micro-diffraction is sensitive to lattice distortion, such as those which are majorly present in the vicinity of the interface. Due to this sensitivity it has the ability to measure the residual strain in the interface zone formed between the alumina and zirconia phase. This micro-residual strain is an indication of the advantage in using a mixture for the second phase. Since the two phases do not mix, some accommodation of each of the constituents properties, such as CTE, results. The residual strain at the interface is identified from line scans which observe the strain at points following the path of the line across the interface. These diffraction measurements are based on elastic displacements of atoms, d, from their equilibrium strain free lattice positions, d_o, according to Bragg's law. At room temperature ceramics deform elastically, $\Delta d = d - d_o$, rather than with elastic and plastic flow commonly observed in metals. Diffraction directly observes the total strain, $\varepsilon = \Delta d / d_o$, in these materials up until failure. In addition, diffraction measurements average over the diffracting grains in an irradiated volume. For materials such as dental ceramics, the grain size (less than 1 μm) is small relative to the beam allowing micro-diffraction measurements to be representative of an isotropic continuum rather than being heavily influenced by individual grains whose grain to grain stress[20] may significantly deviate from the local average.

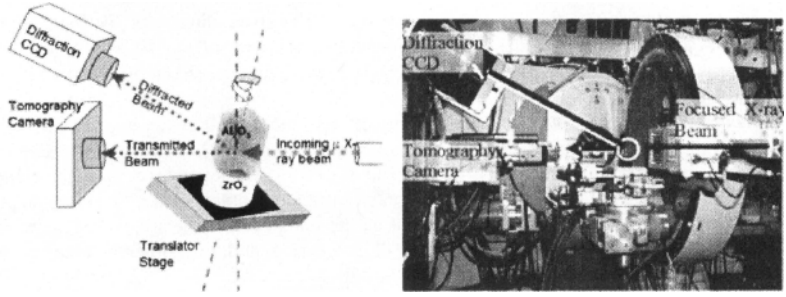

Figure 2. Left, schematic of the diffractometer stage. Right and the labeled photograph (right) show the arrangement of the diffraction and tomography cameras mounted with relation to the incident beam.

Sample alignment and stability is very important since micro-diffraction measurements are sensitive to sample displacement. The error in the measured inter-planar spacing as a result of displacement δ is given by the following equation.[17]

$$\Delta(2\theta) = -\delta \cdot \frac{\sin(2\theta)}{R}; \quad \sigma = -\frac{E}{\upsilon}\frac{\pi}{360}\Delta(2\theta)\cot\theta$$

where, θ is the Bragg angle, R is the Radius of the goniometer. For example, a sample displacement of 100 µm along the beam (as shown in Figure 3) causes an error of 100×10^{-6} in $\Delta 2\theta$, assuming a 100 mm goniometer radius and a 2θ of 30°. This is equivalent to a 20 MPa error in alumina stress. Thus from the equation it is evident that displacement errors can be large.

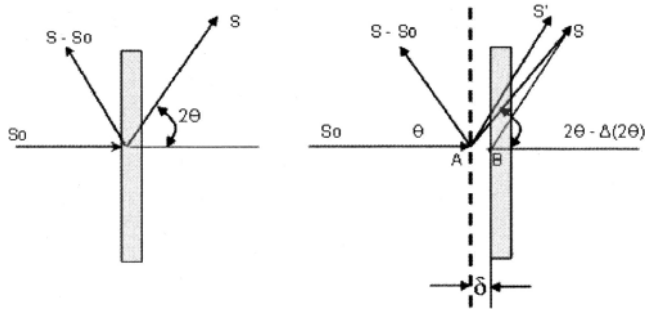

Figure 3. Schematic of displacement error caused when sample is moved with respect to the beam. Reproducibility of the translation stage and alignment of the sample when moving, such as for line scans or d_0 measurements depend on this error being small.

To avoid translation errors in d-spacing, the composite sample and its two strain-free references, one for each layer type, were positioned in-line and checked with 90° in plane, ϕ, rotations to verify alignment. In addition the translations were checked by live radiographs. Periodic recordings of the beam spot and monitoring of the system alignment were documented. To within the resolution of the measurements, translation errors of the entire system were maintained below 10 µm with typical errors for any one exposure much less than 1 µm.

The composite and strain-free reference samples were mounted together and sample switching was done with the use of lateral translation. Monitoring the d-spacing of the strain free references allows corrections for d-spacing changes in the ceramic which are not due to layering in the composite. For example, Yttria stabilization in zirconia or low concentration contaminates in the alumina powder. Keeping these references in the same environment as the composite ensures even the same thermal conditions are maintained for the references. All processing and experimental conditions were maintained identically for these specimens.

Experimental geometry

The diffraction exposures were recorded onto a diffraction CCD (QUANTIX 6303e), oriented at an angle of θ to the incident beam. Since only a small arc (1.2° of the entire diffraction cone) is recorded, only one component of the strain tensor is observed. Precision in θ is paramount. A compromise is required such that the brightest peaks are captured in order to have higher strain accuracies, yet the peaks are clearly resolved to a resolution within ±0.0001° θ (which corresponds to a strain of 10×10^{-6}). A careful choice of the diffraction cone area is made with considerations of low background and interference from other diffracting phases, within the limitations of shadowing from goniometer components and other hardware.

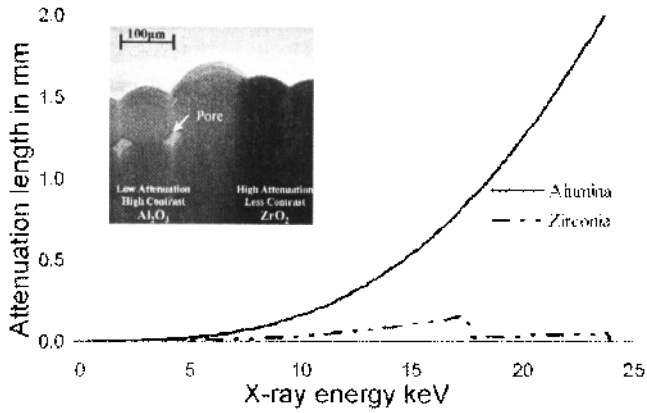

Figure 4 Plot of X-ray attenuation as a function of Energy.[18] The inset shows a typical radiograph and illustrates the difference in X-ray attenuation for the two phases at 21 keV.

It is important to note that the diffracted intensity recorded on the CCD is the result of diffraction from many grains in the sample that lie along the beam path. High-energy synchrotron X-rays, 21 keV, were obtained using the double crystal monochromator. Figure 4 shows the level of attenuation of the beam, caused by alumina and zirconia. With an absorption edge at 18 keV, zirconia absorbs most of the beam. The diffraction signal obtained in the zirconia region is limited to the surface. For transmission the signal is less than 1% in the zirconia region as is evident from the intensity plot and the tomographic section shown in Figure 5.

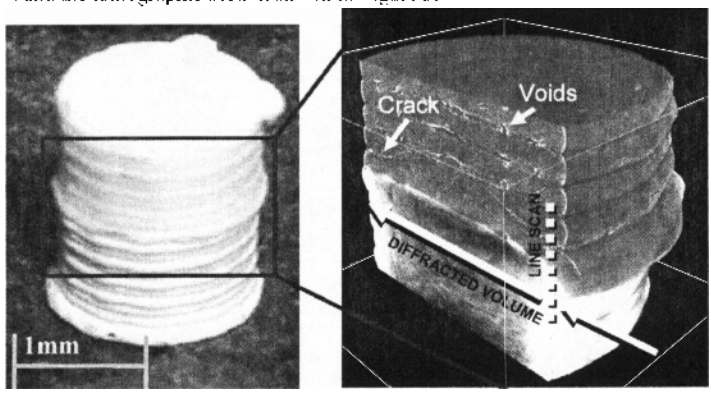

Figure 5 Bi-layer ceramic with alumina on top and zirconia at the bottom (left). Tomographed volume showing detailed features in the cross section

For micro-diffraction, the X-ray beam is focused through a series of compound refractive lenses to a diameter of 14 μm x 7 μm as measured by a radiograph.[19] The lenses were placed several

meters upstream of the center of diffraction. To switch between micro-diffraction and imaging, the compound refractive lenses were translated out of the beam path. This allows the parallel beam through for imaging. Further adjustment of the imaging beam was done with slits. The tomographs were taken with this larger parallel beam which can be adjusted from 2 to 4 mm across.

Diffraction exposures were obtained for each scan point along the dashed line shown in Figure 5. A Lorentzian profile algorithm was used to fit the peaks obtained by binning and integrating the rings. The residual strains were calculated by comparing these peak positions with the value obtained from the strain-free references. The two alumina peaks namely (3 0 0), (2 1 4) which have the strongest signal are used for the strain calculation. Figure 6 shows an example of the CCD exposure giving sections of the rings. The CCD was corrected for distortion by calibrating with a CeO_2 standard powder. For the plot on the right, a series of integrated patterns of ceramic peaks show the change in composition proportional to the change in peak areas as the line scan progresses from the alumina phase to the zirconia phase.

High resolution tomographs consist of a sequence of radiographs taken for 0.25° ϕ steps of the sample about its central axis. The 3D reconstructions were analyzed with various slice orientations (AMIRA 3.1.1 a 3D visualization software). Features like cracks, pores, discontinuities and different phases were observed. The entire tomograph consists of 1024 slices, the total assemblage of all the slices requires 4Gb of memory. Each slice includes 1024 x 1024 pixels. The images were converted to 8-bit TIFF format suitably rescaling the intensity ranges to maintain the contrast between the alumina phase, zirconia phase, the pores, and the crack.

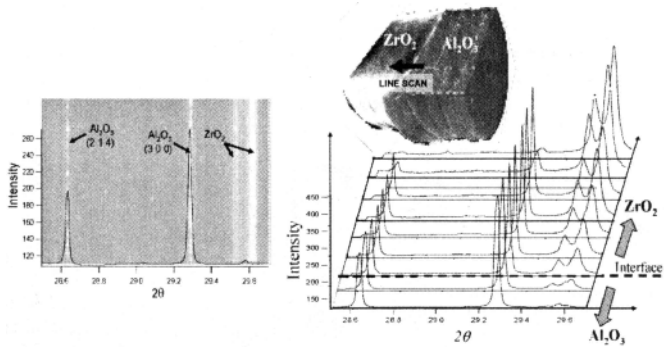

Figure 6 Indexed alumina peaks in the alumina phase. The image on the left is from a scan point close to the interface, hence the ZrO_2 peaks are visible. The plot on the right shows peak profiles approaching the interface.

Tomography to Finite Element Model

An important aim of this experiment was to determine the ability to generate a computational model of the complex geometry of the freeform fabricated sample and simulate the sintering process that results in residual stresses and cracking. Reconstructed data obtained from tomography was digitally visualized in 3D. The different phases can be distinctly seen by the contrast. The material coordinates were registered into a model including the material properties before submitting to finite element analysis. The process of differentiating the constituent phases of the tomography is called segmentation. Segmentation involves a detailed procedure of image processing to reduce noise, and enhance key features like voids, pores, and cracks. Followed by the initial image processing, each

slice was recast, using a threshold to extract basic features on a broader scale. Some low contrast features such as, interface delineations between two phases (as seen in Figure 5) were difficult to segment using the automatic tools, and were selected manually

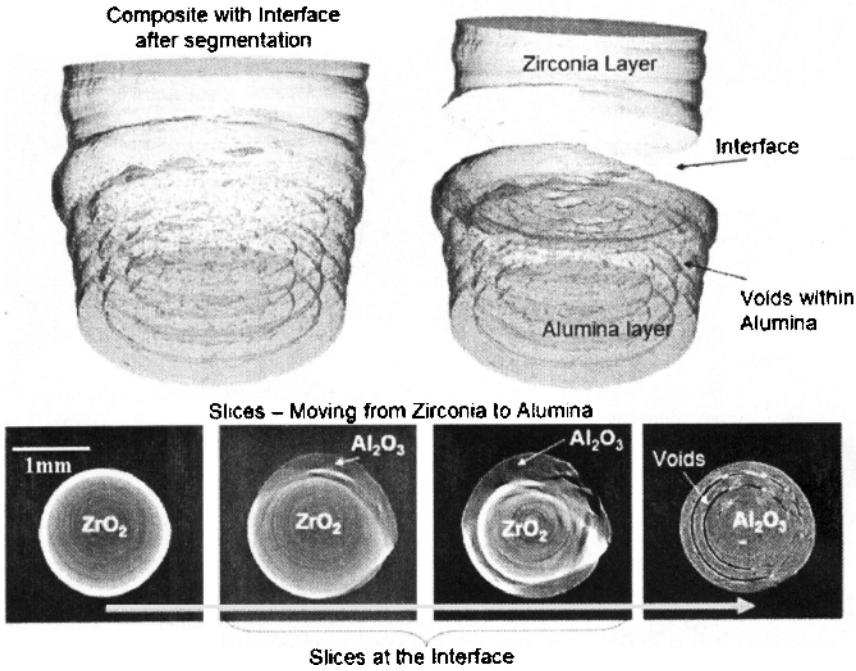

Figure 7 Segmentation of the sample volume based on contrast and threshold intensity. Bottom figures show orthogonal slices moving from the zirconia to the alumina region. Features in the alumina region are clearly seen compared to the zirconia region due to high transmission in the alumina region

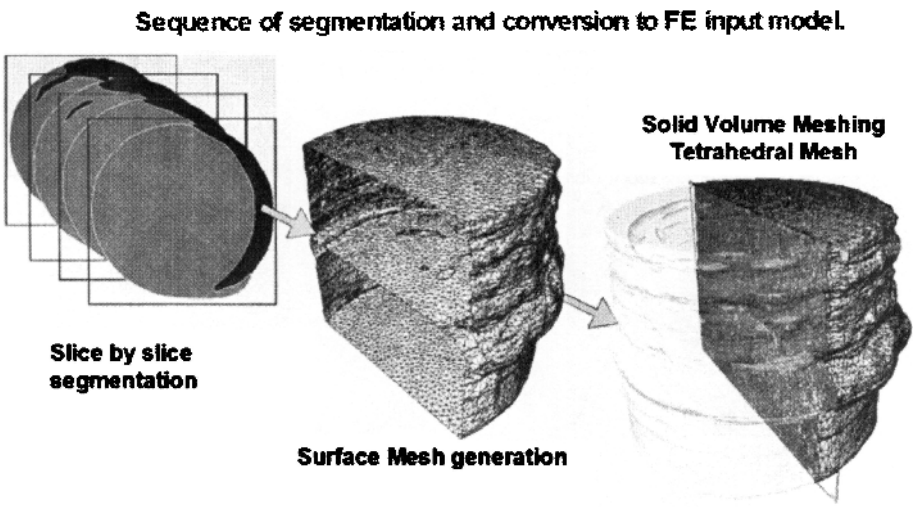

Figure 8 Example images representing steps showing implementation of segmentation, surface, and volume meshing for input to finite element modeling.

The volume is segmented by labeling phases according to the material density. The volume was reconstructed from a subset of 800 slices out of a total of 1024 orthogonal slices. Each slice was segmented based on intensity threshold and contrast. Some example frames are described in Figure 7. Following segmentation, a surface mesh is generated on the material boundaries. The surface mesh creates a well defined closed boundary for the entire sample volume including pores. This is an important step since quality of the surface mesh dictates the quality of the volume mesh generated in the succeeding step. Surface mesh generation is done in steps of gradually decreasing surface elements. The primary goal is to reduce the total surface elements while maintaining the surface geometry. Reduced facets leads to fewer volumetric tetrahedrons generated which reduces demand on computational resources. For example, 1021692 tetrahedrons were employed in our calculations. Reduction from 1,739,702 facets to 50,000 facets was typical. After a successful surface mesh is generated, the marching algorithm[20] fills the volume with tetrahedral of nodal properties corresponding to the material it contains.

FE Analysis

After the volumetric tetrahedral mesh was generated (Amira) the model was exported for post-processing (Hypermesh v7) where mesh validation and refinement operations were done and finally converted to an input format for Finite Element Modeling (FEM), (Abaqus v6.6). The input file has details of nodal properties, interface contact nodes, and spatial information. Figure 9 shows a comparison of the radiograph of the composite and the finite element mesh generated from the tomograph. The region where the diffraction line scan was recorded is depicted. Model orientation with respect to the co-ordinate system was established before the nodal path was assigned. The orientation with reference to the beam was digitally fixed by hand using visual feedback comparing the

oriented mesh with the radiograph. As seen in the Figure 8, a small error in the rotational orientation is possible. However, this has minimal impact on the results since the sample is generally axially symmetric. Automating this step could improve the alignment

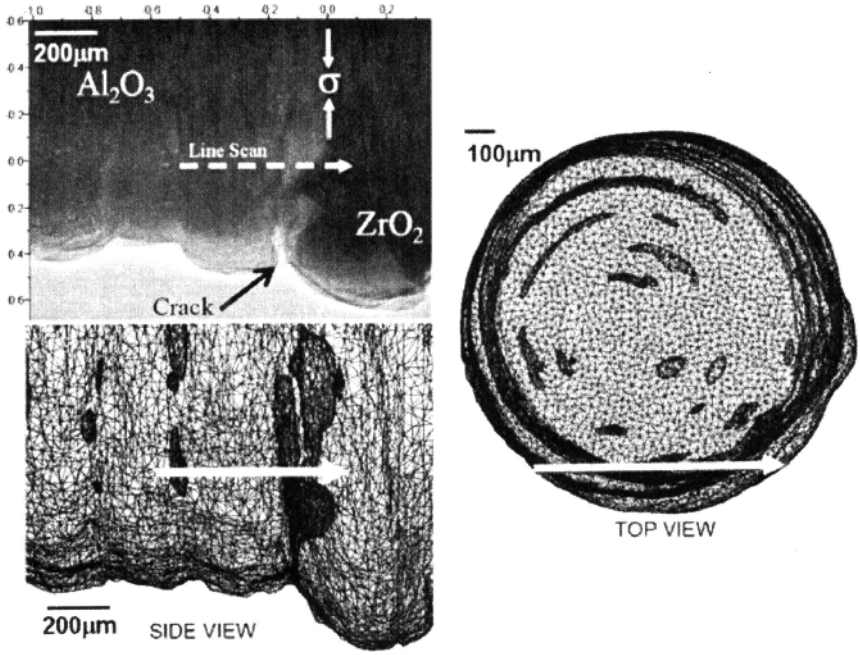

Figure 9. A Comparison of the real sample and the real finite element geometry generated to model residual stress. Left top: Radiograph indicates the position of the X-ray exposures on the sample with respect to the microbeam. Left, bottom: Side view of tetra mesh for FEM. This orientation was used to simulate the strains observed by diffraction. Right: Top view of tetra mesh. This orientation more clearly shows the path of the X-ray beam used for strain measurements.

The FEM code's primary purpose was to conduct the simulation of thermal residual stresses in the composites. The thermal residual stress was simulated in a static general step with 10 incremental steps. The temperature dependant thermal coefficient of expansion for alumina and zirconia is utilized for this analysis[15]. For comparison, an ideal cylindrical Bi-layer composite was also modeled. Material properties corresponding to alumina and alumina-zirconia were initialized at the nodes using region partitioning. The temperature step was applied by defining an initial, 1000°C, and final, 25°C, temperature field around the sample. Average computation time for the complex tomography model and the ideal cylinder model are 12 hours and 1 hour respectively on an Intel Pentium-4 3.20Hz, machine.

RESULTS

The residual strains in the alumina region are compressive as compared to the zirconia region. For the plane parallel to the interface, the X-ray integrated residual strain reaches a maximum of -275 10^{-6} at the interface. Far from the interface, the residual strain relaxes to the strain-free value. The strain falls to half its maximum, 100 μm from the interface. Figure 10 plots these strains as a function of distance from the interface. A radiograph showing the path of the X-ray line scan is also shown. The figure shows registration of the strain data on the corresponding radiograph. The position accuracy is maintained by tracking the coordinates of the micro-beam spot and overlapping the two frames.

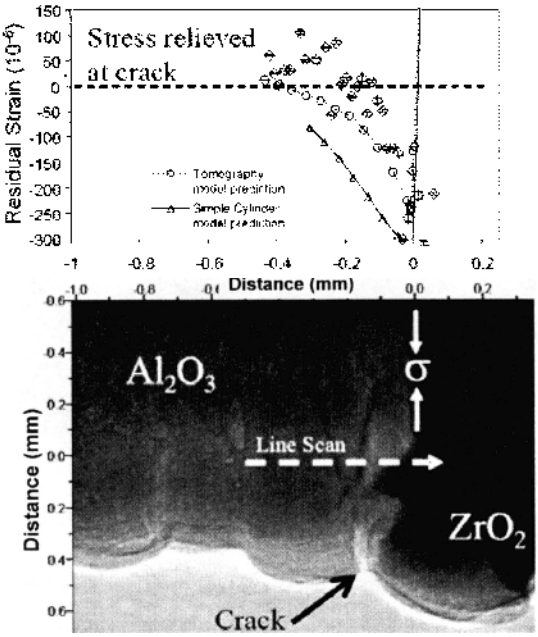

Figure 10 Top: A plot of strains from an X-ray line scan across the interface in the zirconia and alumina layered sample. The plot also consists of the predicted values obtained from FE simulations (ideal cylinder and the real geometry). The measured strains approach zero close to a crack visible in the associated radiograph (bottom). The crack initiates from a notch as a stress concentrator and travels into the alumina phase, terminating within the interior

The residual strains also relax near the crack visible in the radiograph. This crack can be clearly observed in Figure 5 which shows an orthogonal section taken from the tomograph. A crack typical for this sample type was observed. The crack originates from the periphery at a region of stress concentration within the alumina layer and then proceeds away from the interface at an angle of about 30°. The crack appears in the segmentation process as a low absorption gas phase. This crack region was manually filled-in, with the surrounding material properties in the segmentation module for FE

models. Utilizing both the radiograph and the beam-spot position, the line scan region in the FE simulation is also matched to extract results from the same region as done experimentally—an advantage provided by tomography.

Residual strain results for the simple cylinder case are shown in Figure 11. A maximum compressive strain integrated along a path simulating the X-ray beam reached -320 x 10^{-6} at the interface. The strains along the beam path have been integrated to determine a strain value of a volume comparable to that observed with X-ray diffraction. The contour plot obtained from FEM is overlapped with the paths at which the nodal information was gathered. Determining coordinates for a desired node is easy for the simple cylinder case, but becomes challenging for the more complex freeform geometry. To avoid complexities in determining the coordinates of the line scan, a path was defined along a scan point which collects nodal as well as elemental intersection values along the path. The scan path consists of nodes along a pre-defined path and hence only a point region. Whereas in the case of the X-ray diffraction measurement averaging of strains takes place at discrete diffracting grains along a beam path over a volume which contains the area of the beam (14 μm x 7 μm).

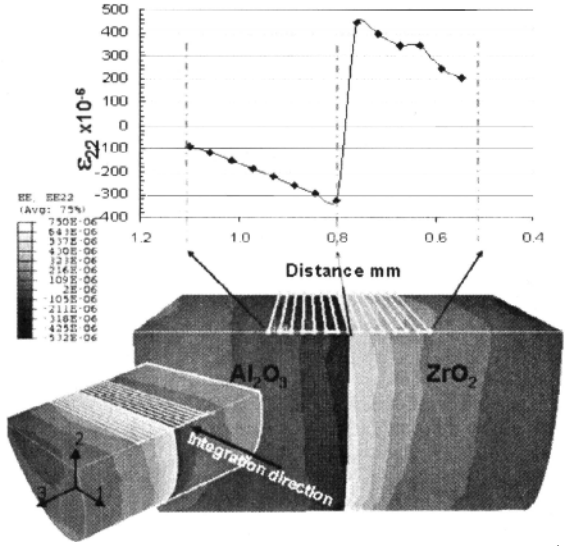

Figure 11 Contour plot showing a section of the ideal cylinder FE simulation of the alumina-zirconia bi-layer composite. The cross-section corresponds to the line scan showing the region through which the strains were integrated. The strains were integrated along the marked paths (white).

Results of the simulation on the tomography based model are shown in Figure 12. A direct comparison between the ideal and the real geometry shows that the real geometry takes into account the voids present as processing defects along with the complex external geometry. It is observed that the integrated maximum compressive residual strain at the interface region is -246 x 10^{-6}, which is lower (almost 70%) than the ideal model case.

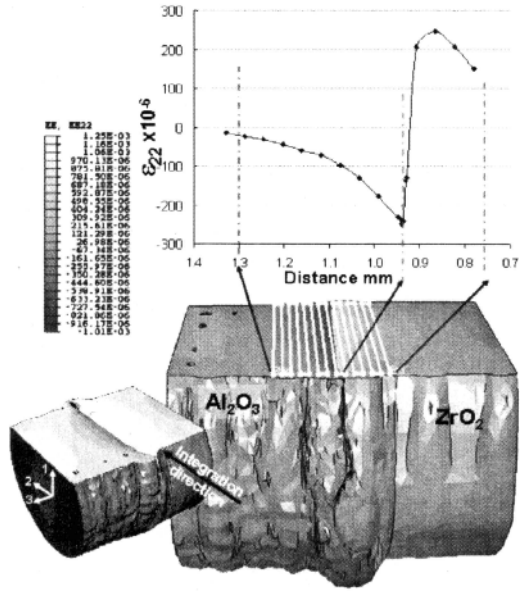

Figure 12 Contour plot showing FE simulation of the alumina-zirconia bilayer composite model based on the real geometry provided from tomography. With the cutaway view, the internal voids and pores in the alumina region are clearly visible.

DISCUSSION

Significant CTE mismatch between the two pure alumina and zirconia layers exists (α_{ZrO_2}=10.9 at 25°C and $\alpha_{Al_2O_3}$= 5.5μm/m-°C at 25°C, 10.1 μm/m-°C at 1127°C),[15] which often results in cracking due to residual stresses. A combined tomography and diffraction measurement leads to precise registration of the scan points on the sample, which pinpoints the location of the measured strains in the context of the local microstructure. At this scale with the presence of defects, accurate registration of the mapped area becomes increasingly critical compared to volumetric measurements or bulk average measurements. It is seen in Figure 6, that as the sample was scanned in the diffraction mode, along line scans running from the alumina region to the zirconia region, the intensities of the zirconia peaks increases and that of alumina decreases gradually. This gradual change is influenced by the integration of the intensities coming from all the grains along a beam path through the sample. Especially at the interface, since the interface is not a flat planar geometry, the beam goes through both the alumina and zirconia grains. However, this X-ray integration of strains across microstructural features is an important aspect regarding interpretation of the residual stress state of the composite.

Without considering the FEM model, the experiments clearly reveal compressive residual stresses exist parallel to the interface in the alumina region and tensile residual stress exist on the zirconia-alumina side of the interface. The highest strain value obtained from the X-ray diffraction was nearly 300 x 10^{-6} at the interface. The compressive strains persist up to 0.2 mm away from the

interface. Where the crack is present, as seen in the radiograph, the strain value was observed to relax. As expected, this relaxation contrasts to the finite element model. The crack was closed for the model to avoid a singularity in the solution and its inability to model large scale deformation as in case of a crack. Crack initiation might be inferred from the stress values in the model which are greater than the yield stress.

An important result of this experiment and the corresponding finite element model is the evaluation of strain values obtained through the integrated grain volume. Since the experiment involves the transmission geometry, diffraction patterns consist of intensities from many grains. Hence, results represent average strain values from many grains in the beam path for a particular scan point, and not from a particular grain. The residual strain values from the experiment were closer to the simulation values for the real geometry simulation than the ideal cylinder case. This is due to the fact that the real geometry simulation not only accounts for the surface morphology, but also takes into account the voids and interface shape, unlike the ideal cylinder. This validation of the finite element model suggests that the model can be used to generate values for the zirconia region which otherwise are difficult to probe with X-rays due to strong absorption.

Conversion of the real geometry to the finite element model through tomography was successfully implemented. The original resolution of the images acquired is far higher than that used in the finite element model. This leads to elimination of voids smaller than 10 microns. Use of higher memory and computational power would overcome this limitation.

CONCLUSION

A comprehensive and effective experimental and computational procedure capable of determining computing thermal residual strains corresponding to pores and phase boundaries such as the layered interface was developed. The computational model generated for an ideal case and a real geometry were validated through experimental results. Generation of the 3D model involved large data volumes. This volume must be carefully reduced without compromising the fine details affecting an analysis. Both the experimental and computational techniques, evaluated a maximum compressive residual strain in the plane of the interface close to 275×10^{-6} due to the coefficient of thermal expansion mismatch. This compressive stress remained up to 0.2 mm into the Alumina layer falling off to the far-field strain-free value, possibly prematurely due to a crack. Since the morphology is complex, these experimental results are aided by comparison with simulations. The validated simulations for the ceramic composite predict principle stresses in excess of 300 MPa at the interface region.

It was shown from simulations that including the real sample geometry was significant in understanding the characteristics of the interface and residual strain state around it. The strain results calculated for an ideal cylinder were nearly 20% greater than the results for the real geometry. The real geometry includes features such as the interface shape, external geometry, and interior voids. The standard deviation of the strains evaluated by micro-diffraction is nearly 10×10^{-6} for the alumina region. The zirconia layer, where strain evaluation using X-rays is more difficult, can be simulated with additional confidence due to the validated model.

ACKNOWLEDGMENTS

The authors are grateful to Diane Rekow and Van Thompson at the NYU Dental College for their guidance and support. In addition, James Smay at Oklahoma State University provided the samples used in this study. A portion of this work was supported by a grant from the National Institutes of Health (NIH-NIDCR, PO1-10976). Yong Chu and Francesco De Carlo provided valuable assistance related to use of the Advanced Photon source. Use of the Advanced Photon Source was

supported by the U. S. Department of Energy, Office of Science, Office of Basic Energy Sciences, under Contract No. W-31-109-ENG-38. The authors also acknowledge a portion of the research results discussed in this publication were made possible by the OHRS award for project number HR07-134, from the Oklahoma Center for the Advancement of Science and Technology.

REFERENCES

[1] B. R. Lawn, A. Pajares, Y. Zhang, Y. Deng, M. A. Polack, I. K. Lloyd, E. D. Rekow, Van P. Thompson, "Materials design in the performance of all-ceramic crowns." *Biomaterials*, Volume 25, Issue 14, June (2004)

[2] W. J. Clegg, K. Kendall, N. Alford, T. Button, J. D. Birchall, "A simple way to make tough ceramics." *Nature*, 347, (1990), 455-457.

[3] C. C. Aydiner, E. Üstündag, B. Clausen, J. C. Hanan, R. A. Winholtz, M. A. M. Bourke, A. Peker, "Residual stresses in a bulk metallic glass–stainless steel composite." *Materials Science and Engineering: A* 399, (2005), 107-113.

[4] N. Daphalapurkar, J. C. Hanan, H. Lu, N. B. Phelps, H. Bale, "Simulation and Tomography of Microstructure Evolution of a Closed-Cell Polymer Foam in Compression." *Mechanics of Advanced Materials and Structures* in press (2007).

[5] D. Bernard, D. Gendron, J.-M. Heintz, S. Bordère , J. Etourneau, "First direct 3D visualisation of microstructural evolutions during sintering through X-ray computed microtomography.". *Acta Materialia* 53 (2005) 121–128

[6] M. D. Demetriou, C. Veazey, J. Schroers, J. C. Hanan, W. L. Johnson, "Expansion evolution during foaming of amorphous metals." Mater. Sci. and Eng. A, (2006).

[7] J. C. Hanan, J. Ma, C. Veasey, H. Lu, M. D. Demetriou, W. L. Jonson, "Microtomography and 3-Dimensional Stresses of Compressed Low-Density Amorphous Metal Foam." *TMSLetters* 3, 1 (2006) 9-10.

[8] H. F. Poulsen, S. Garbe, T. Lorentzen, D. J. Jensen, F. W. Poulsen, N. H. Andersen, T. Frello, R. Feidenhans, H. Graafsma, "Applications of High-Energy Synchrotron Radiation for Structural Studies of Polycrystalline Materials." *J. Synchrot. Radiation*, (1997); 4: 147-154.

[9] E. Nonnet, N. Lequeux, P. Boch, S. L. Colston, P. Barnes " In Situ X-ray Diffraction and Young's Modulus Measurement during Heat Treatment of High-alumina Cement Castables." *J. Am. Ceram. Soc.*, 84 [3] 583–87 (2001)

[10] J. C. Hanan, E. Üstündag, I. J. Beyerlein, G. A. Swift, B. Clausen, D. W. Brown and M. A. M. Bourke, "Elastic Strain Evolution in Single-Fiber Metal Matrix Composites Under Tensile Loading." *Adv. X-Ray Anal.*, 45, 245-250 (2002).

[11] J. C. Hanan, G. A. Swift, E. Üstündag, I. J. Beyerlein, J. D. Almer, U. Lienert and D. R. Haeffner, "Microscale Elastic Strain Evolution Following Damage in Ti-SiC Composites," *Metall. Mater.Trans. A* 33 (12): 3839-3845 Dec. (2002).

[12] J. C. Hanan, H. Bale, J. E. Smay, Y. S. Chu, F. DeCarlo, "Combined Diffraction and Tomography Analyzing Controlled Residual Stress in Solid Freeform Fabrication." *Synchrotron Radiation in Materials Science*, (2006).

[13] P. G. Coelho, E. A. Bonfante, N. R. Silva, M. Cabrera, E. D. Rekow, V. P. Thompson, "Thermal/Mechanical Modeling and Laboratory Testing of Anatomically Correct All-Ceramic Crowns." Composites at Lake Louise, (2007).

[11] J. C. Hanan, J. E. Smay, F. DeCarlo, Y. Chu, "Microtomography of Solid Freeform Fabrication." *Rapid Prototyping*, 12, NO. 2 (2006).

[15] M. Bauccio, ASM Engineered Materials Reference Book, Second Edition, Ed. ASM International, Materials Park, OH (1994). Accessed through www.matweb.com 1-5-2008.

[16] H. A. Bale, J. C. Hanan, N. Tamura, "Average and Grain Specific Strain Resolved in Many Grains of a Composite Using Polychromatic Microbeam X-Rays." *Adv. X-Ray Anal.*, 49, (2006) 369-374.

[17] A. D. Krawitz, *Introduction to Diffraction in Materials Science and Engineering*, John Wiley & Sons Inc; (2001).

[18] B. L. Henke, E. M. Gullikson, J. C. Davis, "X-ray interactions: photoabsorption, scattering, transmission, and reflection at E=50-30000 eV, Z=1-92." *Atomic Data and Nuclear Data Tables* 54 (no.2), 181-342 (1993).

[19] C. G. Schroer, M. Kuhlmann, B. Lengeler, T. F. Günzler, O. Kurapova, B. B. Benner, C. Rau, A. S. Simionovici, A. A. Snigirev, I. Snigireva, "Design and Microfabrication of Novel X-Ray Optics." *Proc. SPIE* 4783, 10-18 (2002).

[20] W.E. Lorensen and H.E. Cline, "Marching cubes: a high resolution 3D surface construction algorithm." *Comput. Graph.* 21 (1987), pp. 163–169.